Letter Vol. 48, No. 24 / 15 December 2023 / Optics Letters 6589

Efficient second-harmonic generation based on off-Γ merging bound states in the continuum

Shiwen Chen,[1,2] Xiaoyu Dai,[1,2] and Yuanjiang Xiang[1,2,*]

[1]School of Physics and Electronics, Hunan University, Changsha 410082, China
[2]Shenzhen Research Institute of Hunan University, Shenzhen 518055, China
*xiangyuanjiang@126.com

Received 1 November 2023; revised 23 November 2023; accepted 27 November 2023; posted 27 November 2023; published 14 December 2023

Ultracompact devices engineered for second-harmonic generation (SHG) hold a significant promise across a diverse spectrum of applications. Here, we propose a merging bound state in the continuum at an off-Γ point in a reciprocal space with the anisotropic materials lithium niobate. Such a merging BIC yields a profound reduction in radiative loss and scattering losses while concurrently exhibiting a substantial enhancement in the quality factor. As a result, we achieved a noteworthy SHG efficiency ($\eta = 3.7\%$) at the incident angle $\theta = 10^\circ$ when the pump intensity $I_0 = 2\,\mathrm{kW/cm^2}$, outperforming alternative nanostructures designed for SHG. This research contributes valuable insights into the feasibility of metadevices founded on the principles of nanoengineering applied to traditional nonlinear crystals. Such advancements hold a considerable promise for the development of compact, high-performance SHG devices across a range of applications.

https://doi.org/10.1364/OL.510932

Bound states in the continuum (BICs) represent a fascinating quantum phenomenon, residing within the continuous spectrum of extended states, despite their counterintuitive properties of perfect spatial localization and theoretically infinite lifetimes [1–3]. In recent years, BICs have gained a considerable attention, owing to their remarkable properties such as highly confined resonances and unbounded Q factors, effectively mitigating radiation losses [4–6]. In the realm of nanophotonics, BICs have emerged as a valuable resource for enhancing light–matter interactions, with applications spanning surface-emitting lasing [7,8], sensor technology [9–11], and nonlinear frequency conversion [12–14]. Typically, in addition to the well-known symmetry-protected BICs (SP-BICs) achieved through symmetry incompatibility, optical BICs can also be classified as the accidental BICs. While SP-BICs are located precisely at the Γ point ($k = 0$) in the Brillouin zone, accidental BICs exhibit distinct characteristics. These accidental BICs are characterized by the existence of a nonzero transverse component of wave vector k, leading to eigenmodes devoid of symmetry protection. Mathematically, these eigenmodes can be expressed as superpositions of various plane waves, and by adjusting parameters of metasurfaces, it becomes possible to generate destructive interference among the plane waves, culminating in the emergence of bounded accidental BIC modes [15,16].

Ideal BICs can be understood as topological defects within the polarization direction defined in a momentum space [17–20]. These defects, referred to as V points, correspond to the vortex centers of polarization fields [21–23]. The topological nature of BICs ensures them with a distinctive property—they can be continuously displaced within a reciprocal space while preserving the system's underlying symmetry. This ability to manipulate BICs' positions allows for the intriguing phenomenon of merging BICs, where multiple BICs converge at the same wave vector [24–26]. The concept of merging BICs is of particular significance, as it offers a practical means to overcome the scattering losses caused by fabrication imperfections or disorders.

The intricate interaction between electromagnetic waves and optical materials gives rise to a multitude of nonlinear optical phenomena, among which second-harmonic generation stands as a prominent example [27–30]. SHG is a process wherein two photons of identical frequency, denoted as ω, coalesce to generate a solitary photon bearing twice the frequency, expressed as 2ω, in adherence to the principle of energy conservation. In general, SHG in nanostructure without the requirement of phase matching can be characterized as

$$\mathbf{P}(2\omega) \propto \int_V \chi^{(2)}(\mathbf{r},\omega)\,[\mathbf{E}_{\mathrm{loc}}(\mathbf{r},\omega)]^2\,\mathrm{d}V, \tag{1}$$

where $\chi^{(2)}(\mathbf{r},\omega)$ is a tensor of second-order nonlinear susceptibility and $\mathbf{E}_{\mathrm{loc}}(\mathbf{r},\omega)$ denotes the local electric field inside the unit cell [31]. In accordance with Eq. (1), our analysis leads to the conclusion that SHG can be significantly amplified through the augmentation of local-field confinement within nanostructures. Lithium niobate (LN) emerges as a particularly promising material, characterized by its exceptional piezoelectric, electro-optic, and nonlinear optical attributes. Consequently, it has found an extensive application in a diverse array of acoustic and optical devices. This is largely attributable to its substantial second-order harmonic coefficients and remarkable broadband transparency, rendering single-crystal LN an exemplary man-made material for SHG [30–37]. A previous study has shown that 0.49% SHG efficiency can be achieved with LN asymmetric cylinders at $I_0 = 3.3\,\mathrm{kW/cm^2}$ [35]. Recently, Liu *et al.* have demonstrated that the SHG efficiency of a LN membrane exhibiting a merging BIC mode at the Γ point can reach 1% at $I_0 = 2\,\mathrm{kW/cm^2}$ [37].

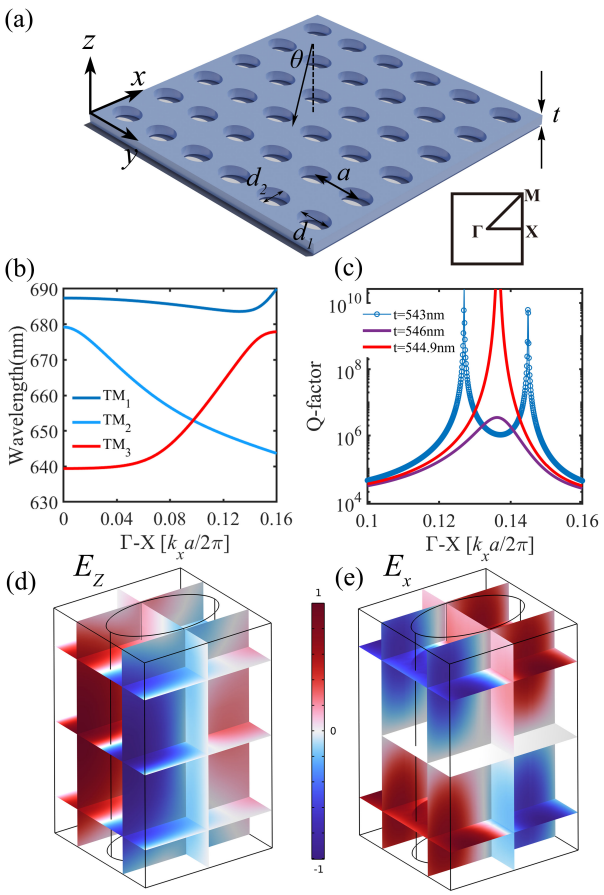

Fig. 1. Design of LN metasurface for merging accidental BICs at off-Γ points. (a) Schematic diagram of a photonic crystal slab with a square lattice of elliptical holes. The lattice constant is $a = 340$ nm, and the major and minor axes of the elliptical hole are $d_1 = 220$ nm and $d_2 = 160$ nm. (b) Calculated TM-like band structure of the slab at $t = 543$ nm related to the BIC mode along the Γ–X direction. The red line is the third TM-like band (TM_3) that we focus on. (c) Variation of Q factor distribution of BIC modes on the TM_3 band along the Γ–X direction for various thicknesses. E_z component (d) and E_x component (e) of the eigenfields corresponding to the BIC mode at $t = 544.9$ nm.

In this Letter, we present a theoretical proposal for a LN photonic crystal slab, which supports two isolated BIC modes along the high symmetry direction Γ–X. Through turning the parameters of the metasurface, we realize a merging BIC mode at the off-Γ point in the k space with anisotropic materials. Furthermore, we numerically investigate the linear properties of the LN slab and achieve an over 400 times the electric field enhancement factor. Ultimately, we show 3.7% conversion efficiency when the pump intensity $I_0 = 2\,\mathrm{kW/cm^2}$. The insights presented in this Letter hold a significant promise for the development of high-efficiency photonic devices based on LN metasurfaces, emphasizing the potential for innovative applications in nonlinear optics and photonics.

Figure 1(a) illustrates a two-dimensional LN membrane, comprising a square lattice of elliptical holes, within a background medium characterized by a low refractive index ($n = 1.46$, commonly employed in laboratory settings). The geometry of a unit cell is determined by several key parameters: the thickness of the membrane (t), the lattice constant (a), and the major (d_1) and minor (d_2) axes of the elliptical holes. The refractive index of lithium niobate is optically anisotropic, featuring distinct values for different crystallographic axes, with $n_y = n_e = 2.18$ and $n_x = n_z = n_o = 2.26$. All the simulations presented in this study have been conducted utilizing a finite-element method (FEM) solver in COMSOL Multiphysics. Bloch boundary conditions are applied in the x and y directions to simulate the periodicity of the structure, while perfectly matched layers have been employed in the z direction to effectively account for wave propagation and absorption phenomena.

Figure 1(b) provides the dispersion of eigenmodes supported by the LN slab along the Γ–X direction. These eigenmodes are distinctly classified as transverse-electric-like (TE-like) or transverse-magnetic-like (TM-like) modes, with, respectively, $H_z = 0$ and $E_z = 0$ at the mirror plane in the z direction. The system also has a C_2 rotation symmetry, time-reversal symmetry (T) and up–down mirror symmetry (σ_h), which altogether ensure that the system supports accidental BICs. By tuning geometry parameters of the system, accidental BICs can be realized along the Γ–X direction, has been further confirmed by the Q factors approaching infinity around $k = 0.128$ and $0.145\,\pi/a$ shown by the blue curve in Fig. 1(c). By increasing the thickness from $t = 543$ nm to $t = 544.9$ nm while maintaining a, d_1, and d_2 unchanged, the accidental BIC is tuned to merge with each other, demonstrating an ultrahigh Q factor over a broad range of wave vectors compared with isolated BICs. By further decreasing t, these two BICs annihilate each other and form a quasi-BIC with a high but not divergent Q factor. We plot the multiple slices of the eigenfields in the z and x directions of the BIC modes in Figs. 1(d)–1(e). Along the Γ–X direction, the TM_3 mode exhibits an odd symmetry for the E_z field with respect to the mirror symmetry σ_d, thus only radiating to S-polarization channel. E_x component of the eigenfields also fits well with the characteristics of TM-like mode.

In order to provide a clear and illustrative representation of the merging process of BICs, we present normalized polarization vector maps within the far field, depicted as white arrows. These maps are accompanied by a color-coded representation of the Q factors, superimposed as the background in the k space. For the Bloch mode with an in-plane wave vector $\boldsymbol{k}_{\parallel} = (k_x, k_y)$ above the light line and below the diffraction limit, the only propagating wave compatible with it is the zero-order Fourier component of Bloch functions. The polarization vector $\boldsymbol{c}(\boldsymbol{k}_{\parallel}) = d_x(\boldsymbol{k}_{\parallel})\vec{x} + d_y(\boldsymbol{k}_{\parallel})\vec{y} + d_z(\boldsymbol{k}_{\parallel})\vec{z}$ with the in-plane wave vector $k_{\parallel}$ can be obtained by

$$\begin{aligned}\boldsymbol{c}\left(\boldsymbol{k}_{\parallel}\right) &= \left[d_x\left(\boldsymbol{k}_{\parallel}\right), d_y\left(\boldsymbol{k}_{\parallel}\right), d_z\left(\boldsymbol{k}_{\parallel}\right)\right] \\ &= \iint_{unit} e^{ik_x x + ik_y y}\boldsymbol{E}\left(x, y, z\right) dxdy \Big/ \iint_{unit} dxdy, \end{aligned} \tag{2}$$

where the unit cell is on an x–y plane above or below the photonic crystal slabs. Figures 2(a)–2(b) present that polarization vector arrows emerge around accidental BICs. The polarization vortex and the Q factor manifest the presence of two accidental BICs. By increasing t, these two accidental BICs with opposite charges gradually approach each other and finally collide at $t = 544.9$ nm, which introduce an ultrahigh Q factor. They can be further seen from projected polarization vector distribution in Figs. 2(c)–2(d), which is represented by the line field tangent to the long axis of the polarization ellipse. The dynamics of these accidental BICs, as they shift along the high symmetry

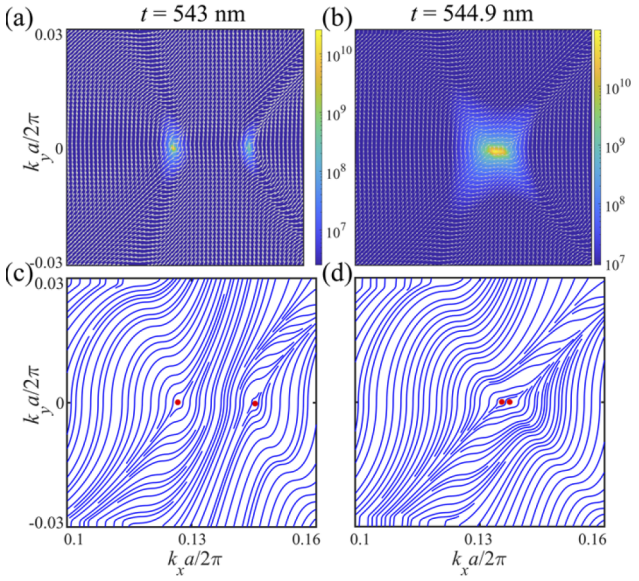

Fig. 2. Dynamic evolution of the topological charges of BIC modes for the TM_3 band at different thicknesses. (a) Simulated normalized polarization vectors (white arrows) for different t of 543 and 544.9 nm, respectively. The background color represents their local Q factors in the momentum space. (b) Calculated projected polarization vector field distribution at $t = 543$ and 544.9 nm, respectively.

Γ–X directions and ultimately merge at t equals 544.9 nm, is strikingly evident through these visual representations.

In order to substantiate our assertion that the novel mechanism under consideration yields pronounced light–matter interactions, thus affording a high-performance SHG, we conducted a rigorous numerical investigation of SHG within a LN slab. In this numerical study, two distinct frequency domain interfaces were established: the first interface, designated for the fundamental frequency (FF), and the second interface tailored for the second-harmonic generation (SH). Notably, these two interfaces were interconnected by the inclusion of polarization features (labeled as **P**), which are

$$\begin{aligned} \mathbf{P}_x^{\mathrm{SH}} &= 2\varepsilon_0[[-d_{22}(E_z^2 - E_x^2) + 2d_{31}E_xE_y]] \\ \mathbf{P}_y^{\mathrm{SH}} &= 2\varepsilon_0[d_{31}(E_z^2 + E_x^2) + d_{33}E_y^2] \\ \mathbf{P}_z^{\mathrm{SH}} &= 4\varepsilon_0[d_{31}(E_zE_y) - d_{22}E_zE_x], \end{aligned} \tag{3}$$

where $d_{22} = 2.1$ pm/V, $d_{31} = -4.6$ pm/V, and $d_{33} = -25.2$ pm/V [31,37]. We used monochromatic FF wave (intensity of 2 kW/cm^2) to excite the metasurfaces, and the SH power is calculated by surface power integration on the output port plane.

Figure 3(a) showcases the simulated transmission spectra of the metasurface with $t = 544.9$ nm under an incident angle of $\theta = 8°$, 10°, and 12°, respectively. Oblique incidence in the *xoy* plane is adopted here to break the in-plane symmetry; thus the ideal BICs transform into quasi-BICs, which enables the BIC mode to couple to its nearby leaky modes. According to the formula $\boldsymbol{k}_{\parallel}{}^2 + \mathbf{k}_z{}^2 = \mathbf{k}_0{}^2\mathbf{n}_0{}^2$, we solve that the merging BIC mode locates at $\theta_{BIC} = 10.7°$. When the incidence angle is closer to θ_{BIC}, the narrower the linewidth of the transmission spectrum, leading to a higher Q factor. To provide further insights into the field enhancements and predict the SHG characteristics, we calculate the electric energy stored within the metasurface at the

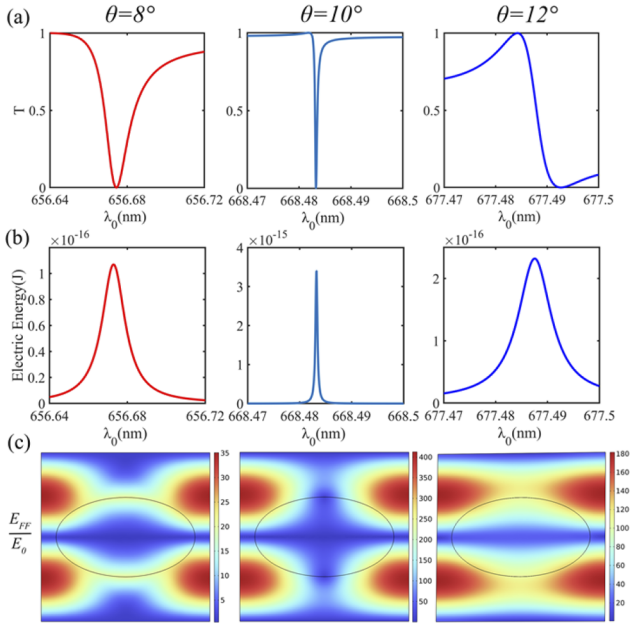

Fig. 3. Transmission spectrum and linear properties of the LN slab. (a) Transmission spectra of the LN metasurface with thickness $t = 544.9$ nm (merging BIC) under various incident angles. (b) Electric energy stored in one unit cell of the LN slab for merging BIC under different incident angles. (c) Enhancement factors of localized FF fields of the merging BIC mode excited under various incident angle.

Table 1. Comparison of SHG Efficiency

Materials	Structure	FF Power (MW/cm^2)	Efficiency η
LN	Waveguide grating [33]	1.3×10^3	8.1×10^{-5}
LN	Elliptical cylinders [34]	5.3×10^3	1.4×10^{-4}
LN	Asymmetric cylinders [35]	3.3×10^{-3}	4.9×10^{-3}
AlGaAs	Nanocavity [36]	1.0×10^3	4.8×10^{-2}
LN	Photonic crystal slab [37]	2.0×10^{-3}	1.0×10^{-2}
LN	Our work	2.0×10^{-3}	3.7×10^{-2}

BIC mode via volume integration of $\vec{\tilde{\epsilon}} \cdot \vec{E} \cdot \vec{E}$ inside an individual unit cell as shown in Fig. 3(b). Notably, the electric energy inside the unit cell under $\theta = 10°$ incidence surpasses that of the other two angles by an order of magnitude, and the quasi-BIC associated with the non-radiative resonance is intrinsically accompanied by a giant field concentration in the resonators. Figures 3(c) illustrates the electric field distribution E_{FF} at the peak wavelength identified in Fig. 3(a) under various incident angles. The electric field distribution depicting the field concentration in the unit cell reveals the non-radiative nature of the quasi-BIC. Remarkably, an electric field enhancement factor exceeding 400 is discernible within the lithium niobate (LN) slab, underscoring the notable field enhancement achieved.

In Fig. 4(a), we present the SHG conversion efficiency ($\eta = P_{SHG}/P_{pump}$, where P_{pump} is the pump power at the fundamental wavelength) with a merging BIC mode under various incident

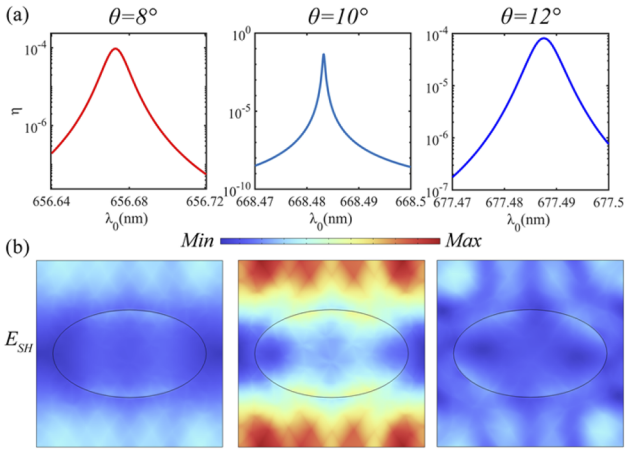

Fig. 4. SHG properties of the LN metasurface. (a) SHG conversion efficiency η for merging BIC under various incident angles. (b) Normalized SH fields of the quasi-BIC mode excited under different incident angles for the LN metasurface.

angles. Notably, under 10° incidence, we achieve a conversion efficiency of 3.7% through the merging BIC mode mechanism when the pump intensity $I_0 = 2\,\mathrm{kW/cm^2}$. This enhanced SHG response is further exemplified by the visibly intensified normalized SH fields associated with the merging BIC under the 10° incidence angle, as contrasted with the other incidence angles, as presented in Fig. 4(b). For a more comprehensive and visual perspective, we compare our results with previous simulations (Table 1), showcasing the superiority of our approach. Notably, our results demonstrate SHG performance that exceeds prior LN metasurfaces supporting isolated modes, designed based on waveguide-grating structures [34], stacked elliptical cylinders [35], and asymmetric elliptical cylinders [36]. Moreover, our results also rival the SHG efficiency of AlGaAs nanocavities [37], while relying on a significantly lower pump power. Under the same merging BIC mechanism, the SHG efficiency η produced by our BIC at the off-Γ point is several times higher than that at the Γ point. These indicate that such merging BIC at the off-Γ point can be an efficient way to boost SHG response.

In this study, we present numerical evidence showcasing the substantial enhancement of SHG conversion efficiency within a LN photonic crystal slab, achieved through the merging BIC mode mechanism at an off-Γ point. We have achieved the merging BIC mode at the off-Γ point with the anisotropic material and the SHG efficiency $\eta = 3.7\%$ when the pump intensity $I_0 = 2\,\mathrm{kW/cm^2}$. Such a high SHG conversion efficiency is useful to realize future integrated nonlinear light sources. Furthermore, such high Q factor structures can also be used in other parametric nonlinear processes, such as sum frequency generation, difference frequency generation, etc.

Funding. Basic and Applied Basic Research Foundation of Guangdong Province (2023A1515011766); Natural Science Foundation of Hunan Province (2021JJ30135, 2021JJ3014); National Natural Science Foundation of China (12247111, 12374302).

Disclosures. The authors declare no conflicts of interest

Data availability. Data underlying the results presented in this paper are not publicly available at this time but may be obtained from the authors upon reasonable request.

REFERENCES

1. H. Friedrich and D. Wintgen, Phys. Rev. A **32**, 3231 (1985).
2. D. C. Marinica, A. G. Borisov, and S. V. Shabanov, Phys. Rev. Lett. **100**, 183902 (2008).
3. A. E. Miroshnichenko, S. Flach, and Y. S. Kivshar, Rev. Mod. Phys. **82**, 2257 (2010).
4. Y. Plotnik, O. Peleg, F. Dreisow, *et al.*, Phys. Rev. Lett. **107**, 183901 (2011).
5. J. Lee, B. Zhen, S.-L. Chua, *et al.*, Phys. Rev. Lett. **109**, 067401 (2012).
6. A. Kodigala, T. Lepetit, Q. Gu, *et al.*, Nature **541**, 196 (2017).
7. C. Huang, C. Zhang, S. Xiao, *et al.*, Science **367**, 1018 (2020).
8. Z. Han and Y. Cai, Opt. Lett. **46**, 524 (2021).
9. J. Lv, Z. Chen, X. Yin, *et al.*, IEEE Photonics J. **12**, 4501610 (2020).
10. X. Zhang, J. Liu, and J. Qin, Nanoscale Adv. **5**, 2210 (2023).
11. D. N. Maksimov, V. S. Gerasimov, S. Romano, *et al.*, Opt. Express **28**, 38907 (2020).
12. D. L. Sounas and A. Alù, Phys. Rev. B **97**, 115431 (2018).
13. L. Kang, Y. Wu, and D. H. Werner, Adv. Opt. Mater. **11**, 2202658 (2023).
14. P. Vabishchevich and Y. Kivshar, Photonics Res. **11**, B50 (2023).
15. C. W. Hsu, B. Zhen, J. Lee, *et al.*, Nature **499**, 188 (2013).
16. C. W. Hsu, B. Zhen, A. D. Stone, *et al.*, Nat. Rev. Mater. **1**, 16048 (2016).
17. B. Zhen, C. W. Hsu, L. Lu, *et al.*, Phys. Rev. Lett. **113**, 257401 (2014).
18. C. W. Hsu, B. Zhen, M. Soljačić, *et al.*, "Polarization state of radiation from a photonic crystal slab," arXiv, arXiv:1708.02197 (2017).
19. Y. Zhang, A. Chen, W. Liu, *et al.*, Phys. Rev. Lett. **120**, 186103 (2018).
20. T. Yoda and M. Notomi, Phys. Rev. Lett. **125**, 053902 (2020).
21. Y. Zeng, G. Hu, K. Liu, *et al.*, Phys. Rev. Lett. **127**, 176101 (2021).
22. M. Liu, C. Zhao, Y. Zeng, *et al.*, Phys. Rev. Lett. **127**, 266101 (2021).
23. Y. Chen, H. Deng, X. Sha, *et al.*, Nature **613**, 474 (2023).
24. J. Jin, X. Yin, L. Ni, *et al.*, Nature **574**, 501 (2019).
25. M. Kang, S. Zhang, M. Xiao, *et al.*, Phys. Rev. Lett. **126**, 117402 (2021).
26. M. Kang, L. Mao, S. Zhang, *et al.*, Light: Sci. Appl. **11**, 228 (2022).
27. A. Fedotova, M. Younesi, J. Sautter, *et al.*, Nano Lett. **20**, 8608 (2020).
28. L. Carletti, A. Locatelli, O. Stepanenko, *et al.*, Opt. Express **23**, 26544 (2015).
29. N. Bernhardt, K. Koshelev, S. J. U. White, *et al.*, Nano Lett. **20**, 5309 (2020).
30. Q. Liu, B. Cheng, M. Chao, *et al.*, Ann. Phys. **533**, 2100255 (2021).
31. Z. Huang, K. Luo, Z. Feng, *et al.*, Sci. China Phys. Mech. Astron. **65**, 104211 (2022).
32. X. Zhang, L. He, X. Gan, *et al.*, Laser Photonics Rev. **16**, 2200031 (2022).
33. F. Ye, Y. Yu, X. Xi, *et al.*, Laser Photonics Rev. **16**, 2100429 (2022).
34. Z. Huang, M. Wang, Y. Li, *et al.*, Nanotechnology **32**, 325207 (2021).
35. L. Kang, H. Bao, and D. H. Werner, Opt. Lett. **46**, 633 (2021).
36. H. K. Gandhi, D. Rocco, L. Carletti, *et al.*, Opt. Express **28**, 3009 (2020).
37. Q. Liu, L. Qu, Z. Gu, *et al.*, Phys. Rev. B **107**, 245408 (2023).